Development of a Finite Element Model to Investigate the Print Path Influence on Strength of Additively Manufactured Open Hole Coupons

Richard Larson[1], Ashley Newman[1], Von Clyde Jamora[1], Sergii G. Kravchenko[2], Oleksandr G. Kravchenko[1]

[1]Old Dominion University, Department of Mechanical and Aerospace Engineering, Composites Modeling and Manufacturing Group, Norfolk, Virginia

[2]Composites Manufacturing and Research Center, Purdue University, 1105 Challenger Ave., West Lafayette, IN 47906

Abstract

With advances in additive manufacturing which allow control of local material orientation the incorporation of holes in anisotropic material presents a design challenge. Since 3D printing allows to control fiber orientation around a hole it creates an opportunity to tailor local fiber orientation to improve mechanical behavior of 3D printed composites. To effectively utilize the manufacturing degrees of freedom enabled by 3D printing requires predictive computational structural damage modeling design tools. The modeling can be used to fully explore the design space and aid in understanding of the structure-property relationships in 3D printed composites and provide insight into the interaction between various damage modes. This study uses finite element progressive damage modeling methodologies to quantify the effects of varying methods of 3D printing around a hole on structural strength and damage tolerance. Models were evaluated for 3D printed discontinuous fiber composite materials and compared with experimental results. The study considered a "print around hole" case, in which continuous fiber direction, upon approaching the hole, becomes tangent to the radius. This print case was evaluated with different diameter holes, as well as different numbers of perimeters printed around the hole.

Introduction

Traditional fabrication processes for composite materials, such as autoclave molding prepreg laminates have geometrical restrictions and are very labor intensive [1]. Injection and compression molded composites allow geometrical complexity, but do not have as desirable material properties as prepreg laminates, due to poor control of fiber orientation [2]. With these disadvantages of conventional manufacturing processes, there is a need for a fabrication process that can create complex geometries yet still retain the control of fiber orientation to achieve the desired material properties.

Fused deposition modeling (FDM) 3D printing is an additive manufacturing (AM) process in which a filament is extruded through a heated nozzle to build an object layer by layer. This process has recently gained interest due to its versatility, ability for rapid prototyping of geometrically complex parts and the ability to create parts which were not previously possible. Generally, the filament used is a thermoplastic, however, composite filaments also exist. Discontinuous-fiber reinforced composites can now be 3D printed by first creating a filament which contains

discontinuous-fibers [3]. Continuous fiber composites can also be 3D printed. Two common methods for printing continuous fiber composites are dual extrusion, in which the fiber and matrix are extruded separately, and nozzle impregnation [4].

The mechanical properties of 3D printed polymer parts have been studied by many authors. Parameters such as printing direction, layer thickness, infill degree and feed rate have a considerable effect on the quality and performance of 3D printed polymer parts [5]–[7]. It's possible that the 3D printing of polymers and polymer matrix composites can induce a high density of interfaces between layers, between filaments, and between inter-phase materials, which brings up concerns about material fracture and failure [8]. Print dependent crack initiation and propagation in 3D printed polymers under single edge notch tension, and it was determined that the print path can have significant effect on damage initiation, propagation and fracture properties. The print paths studied were 45°/-45° and 0°/90° laminates [8]. An open hole tension (OHT) test offers the ability to now study AM specimens in which a print path can have a changing orientation and is also a useful test for observing damage growth.

The process of 3D printing polymer matrix composites opens new possibilities for the design of materials and structures that were previously difficult or not possible. In this paper, experimental methods of tailoring a print path around a hole with a discontinuous fiber composite filament [9] to create OHT specimens will be discussed. Computational models based on continuum damage mechanics methods were used to predict the strength of OHT samples. Results, conclusions, limitations, and ongoing experimental work will be discussed.

Overview of experimental work

Coupon Preparation and Tensile Testing

The Prusa i3 MK3s 3D printer was used to print samples, with Owens Corning's 1.75mm diameter XSTRAND GF30-PA60 filament. This filament consists of glass fiber reinforcement (30% by weight) and polyamide 6 thermoplastic matrix. The coupons were printed at 250-255°C with a plate bed temperature of 90°C at 20 mm/s. All samples printed were 1 inch wide and 7 inches long. The samples were printed with a bead width of 0.4 mm, and a bead height of 0.2 mm.

In order to tailor the print path around the holes in the open hole tension specimens, as shown in Fig. 2, custom G-code was created. The G-code contains information about the coordinates and corresponding commands along the print path for the printer to execute, including the amount of filament to extrude. In order to create the G-code, a parametric script was generated using MATLAB 2019b [10] in which the coordinates of each point in the print path were determined such that the print beads would be evenly spaced. The print path coordinates, along with other printing parameters such as the extrusion multiplier (which controls the bead width) were written to a text file. This MATLAB generated text file was then read by the Prusa i3 MK3s 3D printer, in order to custom print the samples.

Because 3D printing is known to result in significant voids in the final part, which greatly reduces the performance of the material, a secondary compaction process was used to reduce void content in the coupons. After being printed, the coupons were consolidated at 200°C and 80 psi for 30 minutes in order to improve filament adhesion and reduce void content. Two configurations of coupons were tested to evaluate the effect of the hole size and number of print perimeters. Coupons with hole diameters of 8.7 mm and 2 mm were printed, with the print path tailored around the hole (Figure 1). The coupons with an Ø8.7 mm hole were printed with either 6 passes of the print path around the hole. The coupons with a Ø2 mm hole were printed with either 2 passes of the print path around the hole.

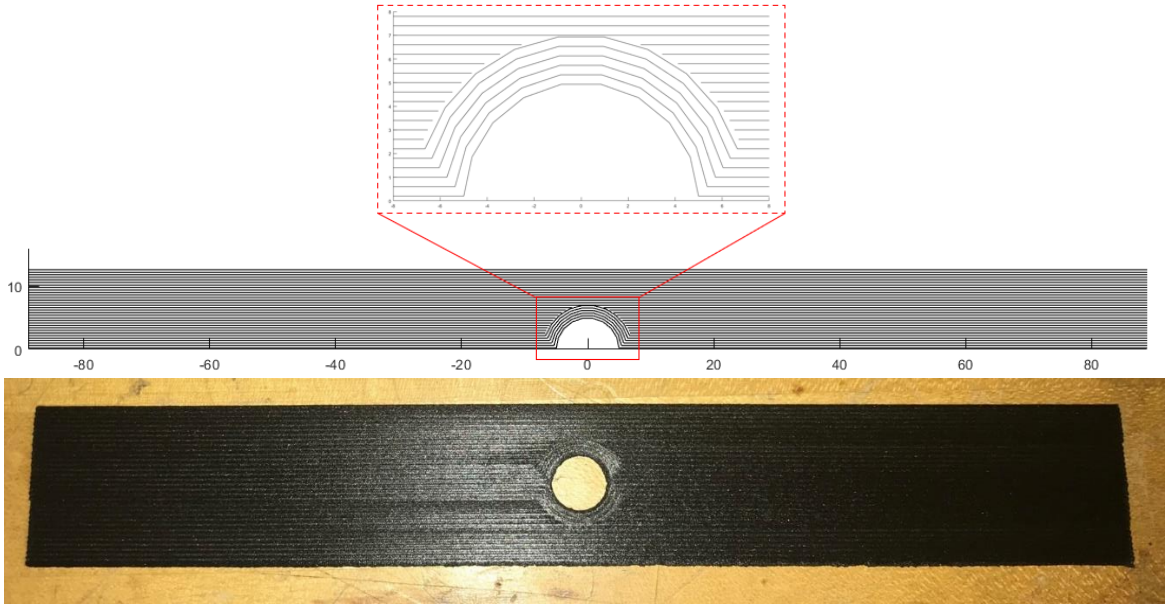

Figure 1 Print path around hole as determined by G-code (top) and experimental OHT sample (bottom).

The coupons were fitted with 1-inch aluminum tabs for the grips of the testing machine. Uniaxial tensile testing was performed using an MTS machine, with 1 mm/min applied displacement. Load and displacement were recorded during the testing. The samples were painted with speckled pattern and strain data was collected via digital image correlation (DIC).

Computational Methods

Parametric Abaqus Model

The coupons were modeled using Abaqus CAE 2018 and solved using Abaqus/Standard. The models were built as parametric Python scripts so that variation of model parameters such as hole radius and number of print radii around hole can be performed with ease. After mesh sensitivity analysis, an element size of 0.15 mm was used. The models contained about 1.7 million elements. To simulate the print path oriented around the hole, the elements around the hole were assigned a material orientation tangent to the radius of the hole (Fig. 2), this was done by using a cylindrical

coordinate system for the elements which were to be oriented around the hole. Material properties used are summarized in Table II.

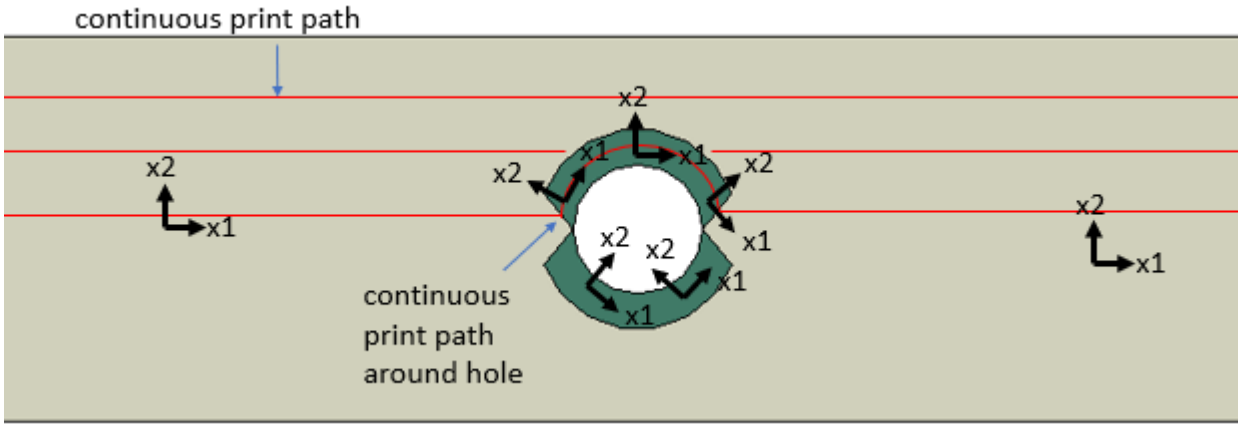

Figure 2. Elements with orientation tangent to hole radius (green).

Table II. Material Properties of XSTRAND GF30-PA60

Material Properties Used	
Youngs Modulus in Longitudinal Direction	7860 MPa
Youngs Modulus in Transverse Direction	4000 MPa
Youngs Modulus Through the Thickness	4000 MPa
Poissons Ratio 1-2	0.38
Poissons Ratio 1-3	0.38
Poissons Ratio 2-3	0.45
Shear Modulus in 1-2 Plane	2000 MPa
Shear Modulus in 1-3 Plane	2000 MPa
Shear Modulus in 2-3 Plane	1380 MPa
Failure Stress in 1 Direction in Tension	106.4 MPa
Failure Stress in 1 Direction in Compression	106.4 MPa
Failure Stress in 2 Direction in Tension	60 MPa
Failure Stress in 2 Direction in Compression	60 MPa
Failure Stress in Shear in 1-2 Plane	50 MPa
Fracture Energy in the Longitudinal Direction	8 N/mm
Fracture Energy in the Transverse Direction	2 N/mm
Viscosity for Regularization in the Longitudinal Direction	0.001
Viscosity for Regularization in the Transverse Direction	0.001
Through the Thickness Strength	60 MPa
Failure Stress in Shear in 2-3 and 1-3 Plane	50 MPa

In order to model the damage initiation and growth a custom user material UMAT subroutine was used. The following are the failure criterion and damage variables used in the progressive damage analysis model:

$$f_1^2 = \frac{(\varepsilon_{11})^2}{\varepsilon_{11}^{f,t}\varepsilon_{11}^{f,c}} + \left(\frac{1}{\varepsilon_{11}^{f,t}} - \frac{1}{\varepsilon_{11}^{f,c}}\right)\varepsilon_{11} = 1$$

$$f_2^2 = \frac{(\varepsilon_{22})^2}{\varepsilon_{22}^{f,t}\varepsilon_{22}^{f,c}} + \left(\frac{1}{\varepsilon_{22}^{f,t}} - \frac{1}{\varepsilon_{22}^{f,c}}\right)\varepsilon_{22} + \left(\frac{1}{\varepsilon_{12}^{f}}\right)^2 (\varepsilon_{12})^2 = 1$$

$$f_3^2 = \left(\frac{\langle\sigma_{33}\rangle}{Z}\right) + \left(\frac{\sigma_{13}}{S_z}\right)^2 + \left(\frac{\sigma_{23}}{S_z}\right)^2 = 1$$

$$d_1 = 1 - \frac{\varepsilon_{11}^{f,t}}{f_1} e^{(-C_{11}\varepsilon_{11}^{f,t}(f_1 - \varepsilon_{11}^{f,t})/G_m)}$$

$$d_2 = 1 - \frac{\varepsilon_{22}^{f,t}}{f_2} e^{(-C_{22}\varepsilon_{22}^{f,t}(f_2 - \varepsilon_{22}^{f,t})/G_m)}$$

$$d_3 = \begin{cases} 0, f_3 < 1 \\ 0.95, f_3 \geq 1 \end{cases}$$

Here 1 indicates the printing direction, 2 indicates the transverse to printing direction, and 3 is the through-the-thickness direction. $\varepsilon_{11}^{f,t}$ and $\varepsilon_{11}^{f,c}$ are the failure strains in the printing direction under tension and compression, respectively. $\varepsilon_{22}^{f,t}$ and $\varepsilon_{22}^{f,c}$ are the failure strains in the transverse direction under tension and compression, respectively. Z and S_z are peel and interlaminar shear strengths, respectively. ε_{12}^{f} is the failure strain in shear.

The stiffness matrix of the damageable composite is:

$$[C] = \begin{bmatrix} (1-d_1)C_{11} & (1-d_1)(1-d_2)C_{12} & (1-d_1)C_{13} & 0 & 0 & 0 \\ & (1-d_2)C_{22} & (1-d_2)(1-d_3)C_{23} & 0 & 0 & 0 \\ & & (1-d_3)C_{33} & 0 & 0 & 0 \\ & & & (1-d_1)(1-d_2)C_{44} & 0 & 0 \\ & & & & (1-d_3)C_{55} & 0 \\ sym & & & & & (1-d_3)C_{66} \end{bmatrix}$$

where:

$C_{11} = \frac{E_{11}(1-\upsilon_{32}\upsilon_{23})}{\Delta}$; $C_{22} = \frac{E_{22}(1-\upsilon_{31}\upsilon_{13})}{\Delta}$; $C_{33} = \frac{E_{33}(1-\upsilon_{21}\upsilon_{12})}{\Delta}$; $C_{12} = \frac{E_{11}(\upsilon_{31}\upsilon_{23}+\upsilon_{21})}{\Delta}$;

$C_{13} = \frac{E_{11}(\upsilon_{31}\upsilon_{23}+\upsilon_{31})}{\Delta}$; $C_{23} = \frac{E_{22}(\upsilon_{31}\upsilon_{12}+\upsilon_{32})}{\Delta}$; $C_{44} = G_{12}$; $C_{55} = G_{13}$; $C_{66} = G_{23}$;

$\Delta = 1 - \upsilon_{21}\upsilon_{12} - \upsilon_{32}\upsilon_{23} - \upsilon_{31}\upsilon_{13} - 2\upsilon_{13}\upsilon_{21}\upsilon_{32}$

More complete details of this continuum damage mechanics based progressive damage analysis model can be found in [11], [12].

Results

Experimental and Computational Comparison

A comparison of the experimental and analysis stress strain curves can be seen in Figure 3. Experimentally, the average peak load for the samples with a Ø2 mm hole and two print paths around the hole, was 78.242 MPa, the computational prediction for this case was 69.728 MPa. The average peak load for the samples with an Ø8.7 mm hole and 6 print paths around the hole was 38.814 MPa, the computational prediction for this case was 49.015 MPa.

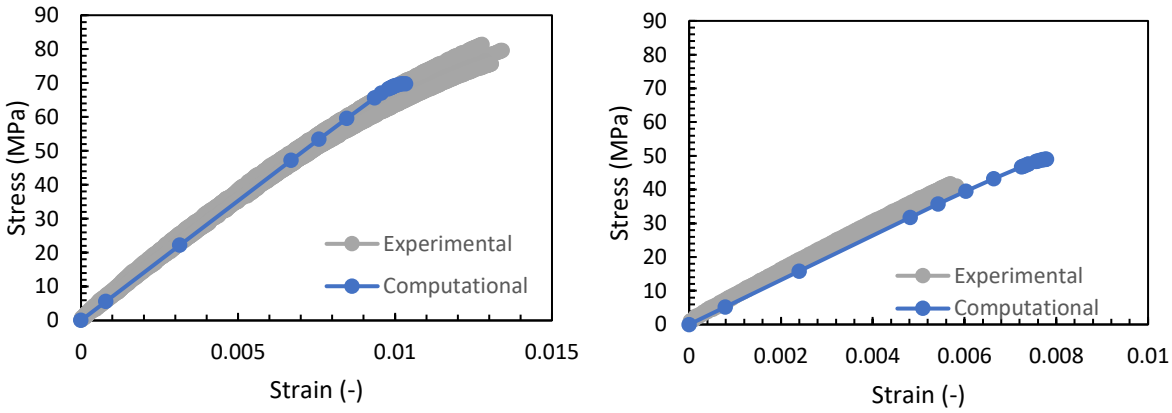

Figure 3. Stress-strain comparison for Ø2 mm hole (left) and for Ø8.7 mm (right).

The damage state at failure was similar for both the Ø2 and Ø8.7 mm hole computational specimens. The damage in printing direction is highest closest to the hole and propagates along the width to the edge of the specimen (Figure 4a). There is a small amount of damage in transverse direction at the crests of the hole which point in the printing direction, and also some transverse direction damage in the at the crests of the hole which align with the width of the specimen (Figure 4b).

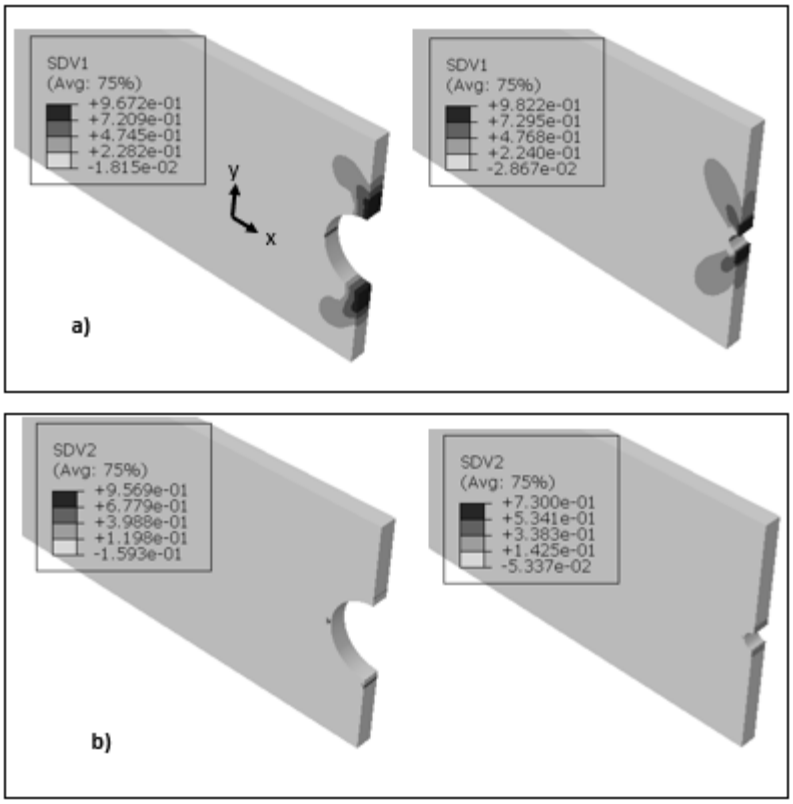

Figure 4. Damage states of experimental configurations at peak load. a) printing direction damage, b) transverse direction damage (Ø8.7 mm hole – left, Ø2 mm hole – right).

The strain concentration profiles at the centerline of the specimen both in the linear loading region and at the peak loads are compared in Figures 5 and 6. Some experimental data points have been removed due to noise in the digital image correlation data. Some computational data points have been removed due to noise caused by elements with high distortion. The strain concentration profiles show an increased strain concentration near the hole in the non-linear load region, compared to the linear load region. The Ø8.7 mm hole linear region strain concentration profile agrees well with the experimental results. The Ø8.7 mm hole non-linear region agrees relatively well with the experimental results, closer to the hole, the strain concentration predicted by the model falls within the range of concentrations observed. The Ø2 mm hole non-linear region strain concentration agrees well with the experimental data. The Ø2 mm hole linear region strain concentration predicted by the model agrees well further away from the hole, but near the hole predicts a lower value than seen experimentally.

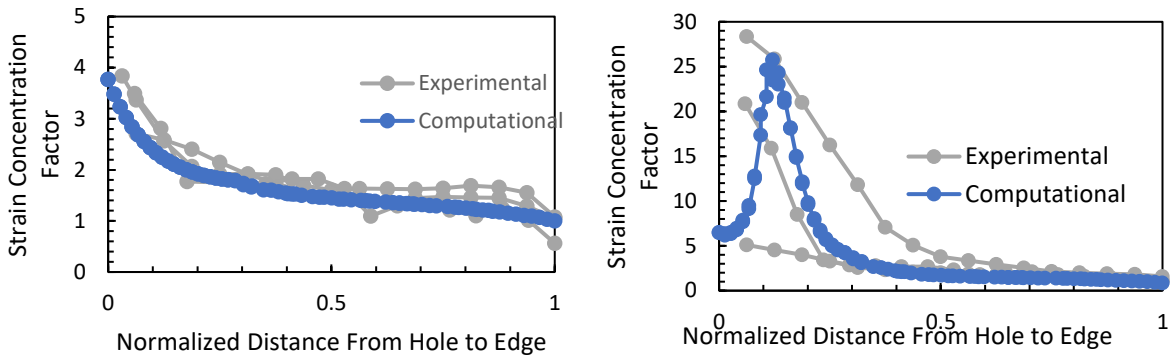

Figure 5. (Left) Strain concentration in linear load region in Ø8.7 mm specimen, (Right) strain concentration at peak load in Ø8.7 mm specimen.

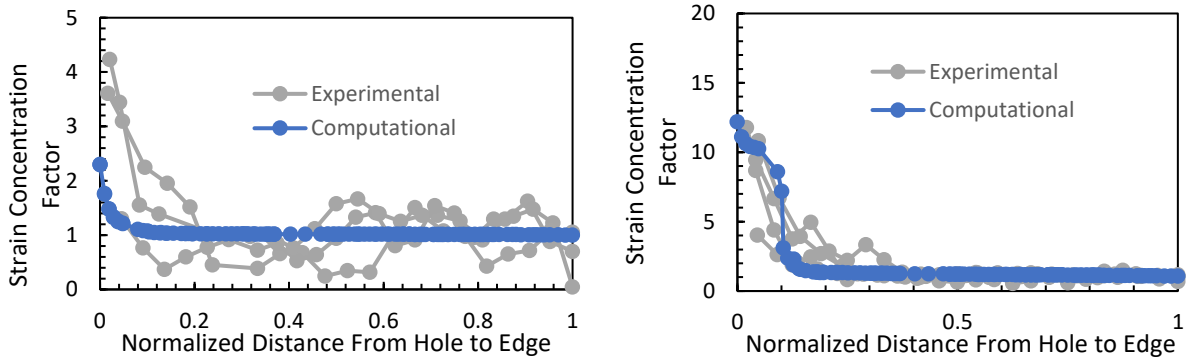

Figure 6. (Left) Strain concentration in linear load region in Ø2 mm specimen, (Right) strain concentration at peak load in Ø2 mm specimen.

The results from the computation study on the effects of number of print radii on the strength of an OHT specimen can be seen for each radius specimen in Figure 7. In the case of the Ø8.7 mmhole, an increased amount of print paths around the hole results in an increased strength prediction. In this case, the sample with 6 print perimeters had a 5% higher peak load compared to the sample with 2 print perimeters. In the case of the smaller Ø2 mm hole, we see that both the 2 and 6 print perimeter cases had a higher peak load than the intermediary 3 print perimeter case.

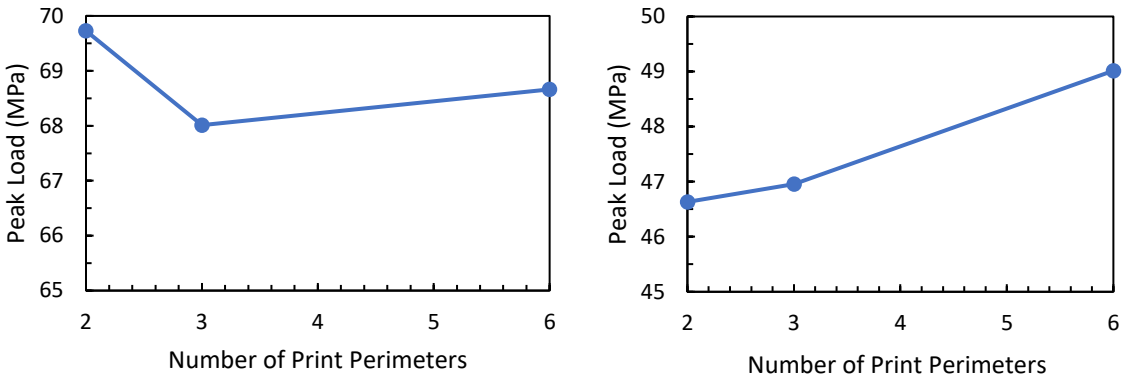

Figure 7 Effect of number of print paths on peak load in Ø2 mm (left) and in Ø8.7 mm (right) hole specimen.

The damage process zone was identified after looking at damage states in all of the models and was captured within the central 40 mm region of the sample. Comparisons of the various damage levels are shown in Figure 8. The percent of elements in the central 40 mm region of the specimens containing various amounts of damage in the printing direction is shown in Figure 9. The specimen with a larger hole had a higher percent of elements with no damage in the print direction, compared to the small hole specimen: the 2, 3 and 6 print perimeter cases of the Ø8.7 mm diameter hole had 92%, 89% and 78% of elements, respectively, whereas the 2 mm hole case for the 2, 3 and 6 print perimeter cases showed 33%, 52% and 45% of elements without damage in the central 40 mm of the specimen. In both cases, more elements with higher levels of damage correlated with a higher peak load. In all cases, very little or no damage in transverse direction and through-the-thickness damage were observed at the peak load. The 8.7 mm 6 print path sample showed 0.0035% of elements in the central 40 mm region with through the thickness damage, the 2 mm 6 print path sample showed 0.002%, and the 2 mm 3 print path sample had 0.0018%.

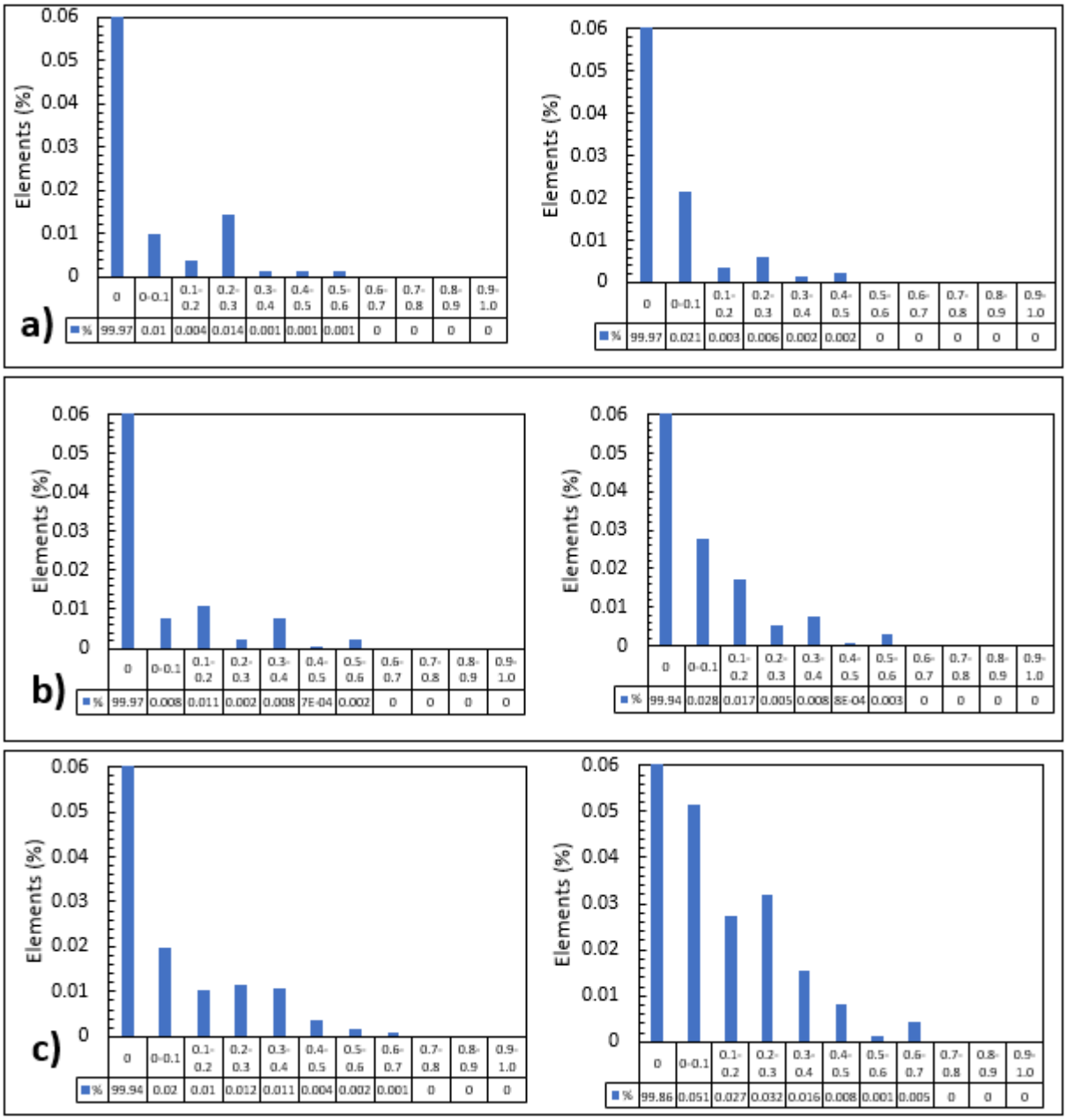

Figure 9. Transverse damage occurrence in center 40 mm of computational specimens. a) 2 print path case. b) 3 print path case. c) 6 print path case (Left) Ø2 mm specimens (Right) Ø8.7 mm specimens.

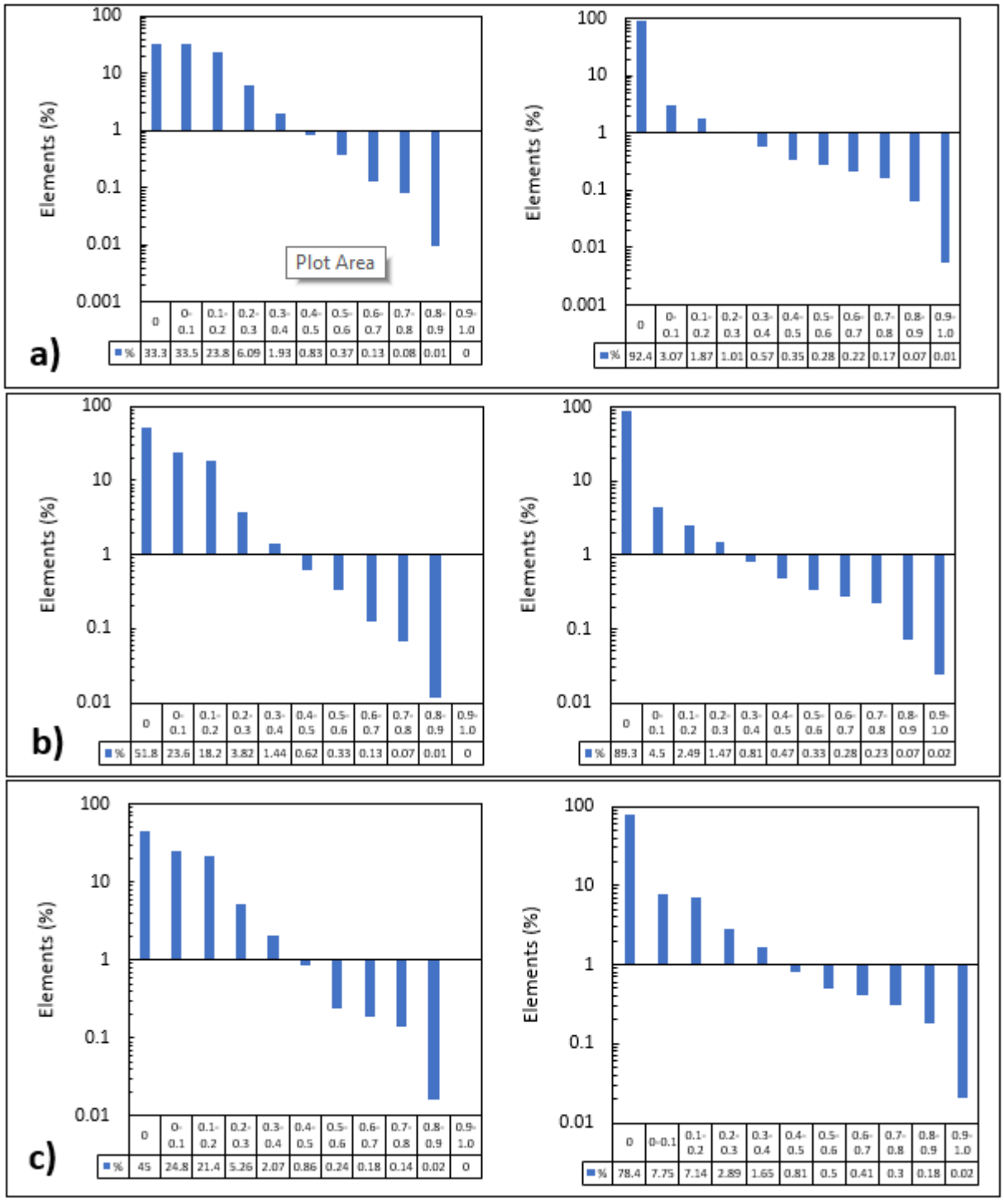

Figure 10. Printing direction damage occurrence in center 40 mm of computational specimens. a) 2 print path case. b) 3 print path case. c) 6 print path case (Left) Ø2 mm specimens (Right) Ø8.7 mm specimens.

Conclusions

The discrepancies observed between the experimental and computational stress-strain curves indicate the need for model improvement. These discrepancies could also be caused by the experimentally observed differences in the amount of consolidation of experimental samples. In the case of the Ø8.7 mm hole specimens, the average ratio of unconsolidated thickness to consolidated thickness was 91.4%, whereas for the Ø2 mm specimens, this average ratio was 86.2%. Microscopy will need to be performed in order to evaluate the effects of the different degree of consolidation on the fiber alignment and void content in the samples. The non-linearity observed in the Ø2 mm experimental stress-strain curve may be a result of delamination cracks forming, which may be better captured by the use of cohesive zone modeling in the analysis, as a limitation of the current model is that it does not model the through-thickness damage progressively.

The number of printing perimeters does not seem to have a significant effect on the strength of OHT sample with 0^o printing configuration and the strength variation is within 3-5% for small (Ø2mm) and large (Ø8.7mm) hole respectively. Samples with a drilled hole will be useful for future work as a baseline with which to compare samples with varying number of print paths around the hole.

Acknowledgements

Richard Larson is acknowledging the support of the NSF Scholarship in STEM (Award # 1833896).

References

[1] O. Ishai and I. Daniel, "Engineering Mechanics of Composite Materials," in *Engineering Mechanics of Composite Materials*, 2nd Edition., New York: Oxford Press, p. 37.

[2] B. Astrom, "Manufacturing of Polymer Composites," in *Manufacturing of Polymer Composites*, 1st Edition., Champan and Hall, p. 301.

[3] T. Hofstätter, D. B. Pedersen, G. Tosello, and H. N. Hansen, "State-of-the-art of fiber-reinforced polymers in additive manufacturing technologies," *Journal of Reinforced Plastics and Composites*, vol. 36, no. 15, pp. 1061–1073, Aug. 2017, doi: 10.1177/0731684417695648.

[4] H. Prüß and T. Vietor, "Design for Fiber-Reinforced Additive Manufacturing," *J. Mech. Des*, vol. 137, no. 11, Nov. 2015, doi: 10.1115/1.4030993.

[5] C. Koch, L. Van Hulle, and N. Rudolph, "Investigation of mechanical anisotropy of the fused filament fabrication process via customized tool path generation," *Additive Manufacturing*, vol. 16, pp. 138–145, Aug. 2017, doi: 10.1016/j.addma.2017.06.003.

[6] H. Li, T. Wang, Q. Li, Z. Yu, and N. Wang, "A quantitative investigation of distortion of polylactic acid/PLA) part in FDM from the point of interface residual stress," *Int J Adv Manuf Technol*, vol. 94, no. 1, pp. 381–395, Jan. 2018, doi: 10.1007/s00170-017-0820-1.

[7] T. D. McLouth, J. V. Severino, P. M. Adams, D. N. Patel, and R. J. Zaldivar, "The impact of print orientation and raster pattern on fracture toughness in additively manufactured ABS," *Additive Manufacturing*, vol. 18, pp. 103–109, Dec. 2017, doi: 10.1016/j.addma.2017.09.003.

[8] J. Li, S. Yang, D. Li, and V. Chalivendra, “Numerical and experimental studies of additively manufactured polymers for enhanced fracture properties,” *Engineering Fracture Mechanics*, vol. 204, pp. 557–569, Dec. 2018, doi: 10.1016/j.engfracmech.2018.11.001.
[9] A. Newman, “Tailoring Printing Orientation Around a Circular Notch in 3D Printed Short-Fiber Reinforced Composites.”, Master’s Thesis, Old Dominion University, 2020.
[10] *MATLAB*, 2019b, Natick, MA: MathWorks.
[11] S. G. Kravchenko *et al.*, “Tensile properties of a stochastic prepreg platelet molded composite,” *Composites Part A: Applied Science and Manufacturing*, vol. 124, p. 105507, Sep. 2019, doi: 10.1016/j.compositesa.2019.105507.
[12] P. Linde, J. Pleitner, H. Boer, and C. Carmone, “Modelling and Simulation of Fibre Metal Laminates,” *ABAQUS Users’ Conference*, Jan. 2004.